Complex Spatiotemporal Modulations and Non-Hermitian Degeneracies in math xmlns="http://www.w3.org/1998/Math/MathML" display="inline" overflow="scroll">mrow>mi mathvariant="script">P/mi>mi mathvariant="script">T/mi>/mrow>/math>-Symmetric Phononic Materials

M. Moghaddaszadeh, M.A. Attarzadeh, A. Aref, and M. Nouh

Phys. Rev. Applied **18**, 044013 — Published 6 October 2022

DOI: 10.1103/PhysRevApplied.18.044013

Complex spatiotemporal modulations and non-Hermitian degeneracies in PT-symmetric phononic materials

M. Moghaddaszadeh[1,2], M. A. Attarzadeh[2], A. Aref[1], and M. Nouh[2*]
[1]*Department of Civil, Structural and Environmental Engineering,*
University at Buffalo (SUNY), Buffalo, NY 14260-4300, USA
[2]*Department of Mechanical and Aerospace Engineering,*
University at Buffalo (SUNY), Buffalo, NY 14260-4400, USA

Unraveling real eigenfrequencies in non-Hermitian $\mathcal{PT}$-symmetric Hamiltonians has opened new avenues in quantum physics, photonics, and most recently, phononics. However, the existing literature squarely focuses on exploiting such systems in the context of scattering profiles (i.e., transmission and reflection) at the boundaries of a modulated waveguide, rather than the rich dynamics of the non-Hermitian medium itself. In this work, we investigate the wave propagation behavior of a one-dimensional non-Hermitian elastic medium with a universal complex stiffness modulation which encompasses a static term in addition to *real* and *imaginary* harmonic variations in both space and time. Using plane wave expansion, we conduct a comprehensive dispersion analysis for a wide set of sub-scenarios to quantify the onset of complex conjugate eigenfrequencies, and set forth the existence conditions for gaps which emerge along the wavenumber space. Upon defining the hierarchy and examining the asymmetry of these wavenumber gaps, we show that both the position with respect to the wavenumber axis and the imaginary component of the oscillatory frequency largely depend on the modulation type and gap order. Finally, we demonstrate the coalescence of multiple Bloch-wave modes at the emergent exceptional points where significant direction-dependent amplification can be realized by triggering specific harmonics through a process which is detailed herein.

I. INTRODUCTION

Modulating the properties of elastic media, whether in lattice or continuum form has been a growing topic of interest in the field of phononic materials [1]. In its simplest form, a phononic crystal represents a composite periodic structure of two or more materials with different properties, which give rise to frequency bandgaps as a result of Bragg scattering and destructive interferences [2]. This discrete periodic alternation of materials represents the most basic form of spatial material modulation. However, phononic crystals with harmonically-varying stiffness profiles represent a different form of continuous modulation where the material change along the spatial coordinate follows a prescribed function, e.g., a sinusoid [3, 4]. Lately, the ability to achieve wave filtering using temporal modulations of material properties via real time-periodic functions has been demonstrated [5, 6], and the notion of spatiotemporal modulations has been theoretically and experimentally utilized to break Lorentz symmetry and instigate nonreciprocal wave transmission. These space-time-periodic systems have ranged in implementation from phononic crystals [7–9] and locally resonant metamaterials [10–12], to stimuli-responsive materials [13]. While stiffness is typically the modulation property of choice, given its accessibility and potential experimental tunability, similar studies have looked into the modulation of other inertial properties including mass [14, 15] and angular momentum in gyroscopic structures [16]. While all the previous efforts rely on real modulation of material property, the concept of using non-Hermitian modulations has been recently adopted particularly in stiffness-modulated waveguides in the form of imaginary harmonic spatial functions [17]. Given the fact that such non-Hermitian modulations are invariant under the action of parity and time reversal operators, the resultant structures are deemed to be $\mathcal{PT}$-symmetric.

$\mathcal{PT}$-symmetric non-Hermitian Hamiltonians, which are capable of possessing real energy spectra, were initially conceived of in quantum physics [18]. There, a sudden phase transition from the exact to the broken region (or vice versa) was realized by passing a critical threshold in which two eigenvalues and their corresponding eigenvectors coalesce, commonly known as the exceptional

---

[*] Corresponding author: mnouh@buffalo.edu

point degeneracy [19]. In the broken phase, eigenvalues emerge as complex conjugate pairs in which modes with positive and negative imaginary components experience exponential amplification and attenuation, respectively. Given the similarity between the Schrdinger equation in quantum mechanics and the wave equation, $\mathcal{PT}$-symmetry was readily extended to optics [20–23], acoustics [24–26] and elastic systems [27–29], primarily through "gain-loss energy pumping mechanisms" via an odd, imaginary form of modulation. Notable among these are the realizations of unidirectional reflectionless absorbers [30], microring lasers [31, 32], dynamic power oscillations [33, 34], nonreciprocal light propagation [35], and invisible acoustic sensors [36]. In the photonics domain, different approaches have been undertaken to implement $\mathcal{PT}$-symmetric optical systems, including aperiodic temporal modulation [37], dynamic gain-loss modulation [38, 39], and Floquet systems [40, 41]. However, $\mathcal{PT}$-symmetric phononic systems have been significantly less explored and limited to space-periodic modulations. In these systems, an imaginary stiffness modulations of an elastic medium becomes equivalent to a cycle of negative (gain) and positive (loss) damping terms in the motion equations which can be experimentally enacted via negative and positive resistive shunt circuits attached to piezoelectric patches which are bonded to the elastic medium, along with a negative capacitance which amplifies the gain and loss effect as needed [42]. Additionally, there remains a large gap between the dynamics, response and behavior of $\mathcal{PT}$-symmetric systems on one hand, and the wave dispersion patterns that culminate from different modulation forms on the other. To date, the vast majority of efforts have primarily focused on leveraging the features of such systems in the context of scattering properties at the boundaries and downstream of modulated waveguides, with little to no attention to the wave propagation profile inside the medium itself.

The current work aims to address the aforementioned questions by providing a comprehensive treatment of spatiotemporal stiffness modulations of an elastic medium, ranging from purely real to complex modulations which are used to exploit non-Hermitian degeneracies in $\mathcal{PT}$-symmetric phononic systems. We start by deriving a unifying theory that employs the plane wave expansion approach to evaluate the dispersion relations of a one-dimensional slender bar, in which the stiffness profile is modulated using a universal, complex spatiotemporal waveform. Developing the analytical framework for the most general case enables us to investigate the dispersion properties for a number of interesting sub-scenarios and draw comparisons between $\mathcal{PT}$-symmetric systems with different modulation forms, by extracting insight from the evolution of the so-called wavenumber gaps, their existence conditions, and their unique behavior associated with the different scenarios. Towards the second half of the paper, we evaluate the effect of the modulation's parameters on both the location and properties of the emergent exceptional points (EPs), by studying and quantifying the directional amplification taking place at such EPs in the presence and absence of temporal modulation of material property. The ensuing analysis interestingly shows that directional amplification of select EPs in time-periodic elastic systems can only be triggered by an input excitation whose frequency signature represents a specific function of the modulating frequency, as will be detailed.

II. THEORY

To study elastic wave dispersion in a continuous system with non-Hermitian space-time modulation, we start with the one-dimensional wave equation governing the structural dynamics of an elastic longitudinal bar, given by

$$\frac{\partial}{\partial x}\left[E(x,t)\frac{\partial u(x,t)}{\partial x}\right] = \frac{\partial}{\partial t}\left[\rho(x,t)\frac{\partial u(x,t)}{\partial t}\right] \tag{1}$$

where $u(x,t)$ describes the bar's displacement at a field point x and a time instant t, and is denoted u hereafter for simplicity. $E(x,t)$ and $\rho(x,t)$ represent the space- and time-dependent elastic modulus and mass per unit length, respectively. The non-Hermitian modulations of the bar's elastic modulus and density are given by

$$E(x,t) = E_o\left[1 + \alpha\cos(\omega_p t - \kappa_p x) + \mathrm{i}\beta\sin(\omega_p t - \kappa_p x)\right] \tag{2a}$$

$$\rho(x,t) = \rho_o\left[1 + \alpha\cos(\omega_p t - \kappa_p x) + \mathrm{i}\beta\sin(\omega_p t - \kappa_p x)\right] \tag{2b}$$

where E_o and ρ_o represent the average modulus and density values, $\mathrm{i} = \sqrt{-1}$ is the imaginary unit, ω_p is the temporal modulation frequency, and κ_p is the spatial modulation frequency. The coefficients

α and β dictate the depth of the real and imaginary spatiotemporal modulations, respectively.

Owing to the periodicity of E and ρ in both space and time, both can be rewritten via Fourier expansions as follows:

$$E(x,t) = \sum_{r=-\infty}^{\infty} E_r \mathrm{e}^{\mathrm{i}r(\omega_p t - \kappa_p x)} \tag{3a}$$

$$\rho(x,t) = \sum_{r=-\infty}^{\infty} \rho_r \mathrm{e}^{\mathrm{i}r(\omega_p t - \kappa_p x)} \tag{3b}$$

The Fourier coefficients E_r of the elastic modulus are given by

$$\begin{aligned} E_r = \frac{\omega_p}{2\pi}\frac{\kappa_p}{2\pi} \int_0^{\frac{2\pi}{\omega_p}} \int_0^{\frac{2\pi}{\kappa_p}} \Re\big(E(x,t)\big)\, \mathrm{e}^{-\mathrm{i}r(\omega_p t - \kappa_p x)}\, dx\, dt \\ + \mathrm{i}\frac{\omega_p}{2\pi}\frac{\kappa_p}{2\pi} \int_0^{\frac{2\pi}{\omega_p}} \int_0^{\frac{2\pi}{\kappa_p}} \Im\big(E(x,t)\big)\, \mathrm{e}^{-\mathrm{i}r(\omega_p t - \kappa_p x)}\, dx\, dt \end{aligned} \tag{4}$$

with the operators $\Re(\bullet)$ and $\Im(\bullet)$ returning the real and imaginary parts of their arguments, respectively. Substituting Eq. (2a) into (4) gives

$$\begin{aligned} E_r = E_o\frac{\omega_p}{2\pi}\frac{\kappa_p}{2\pi} \int_0^{\frac{2\pi}{\omega_p}} \int_0^{\frac{2\pi}{\kappa_p}} \big[1 + \alpha\cos(\omega_p t - \kappa_p x)\big]\, \mathrm{e}^{-\mathrm{i}r(\omega_p t - \kappa_p x)}\, dx\, dt \\ + \mathrm{i}E_o\frac{\omega_p}{2\pi}\frac{\kappa_p}{2\pi} \int_0^{\frac{2\pi}{\omega_p}} \int_0^{\frac{2\pi}{\kappa_p}} \big[\beta\sin(\omega_p t - \kappa_p x)\big]\, \mathrm{e}^{-\mathrm{i}r(\omega_p t - \kappa_p x)}\, dx\, dt \end{aligned} \tag{5}$$

which, following several mathematical manipulations, further simplifies to

$$E_r = E_o\left[\delta_r + \frac{\alpha}{2}(\delta_{r-1} + \delta_{r+1}) + \frac{\beta}{2}(\delta_{r-1} - \delta_{r+1})\right] \tag{6}$$

where δ_r is Dirac-delta function which is equal to unity for $r = 0$ and zero otherwise. With the focus here being on stiffness-modulated structures, we set $\rho(x,t) = \rho_o$ as an invariant parameter and therefore the Fourier coefficient corresponding to the constant density can be defined as $\rho_r = \rho_o\delta_r$. By incorporating the Floquet theorem and implementing the plane wave expansion (PWE) method [43], a solution of the following form is realized:

$$u(x,t) = \mathrm{e}^{\mathrm{i}(\omega t - \kappa x)} \sum_{s=-\infty}^{\infty} u_s \mathrm{e}^{\mathrm{i}s(\omega_p t - \kappa_p x)} \tag{7}$$

where u_s is the amplitude of the s-harmonic in the assumed solution. Upon substituting Eqs. (3) and (7) back into (1), and canceling out the $\mathrm{e}^{\mathrm{i}(\omega t - \kappa x)}$ term, the following equality can be obtained:

$$\sum_{r=-\infty}^{\infty}\sum_{s=-\infty}^{\infty} \kappa_{[r+s]}\kappa_{[s]} E_r u_s \mathrm{e}^{\mathrm{i}(r+s)(\omega_p t - \kappa_p x)} = \sum_{r=-\infty}^{\infty}\sum_{s=-\infty}^{\infty} \omega_{(r+s)}\omega_{(s)} \rho_r u_s \mathrm{e}^{\mathrm{i}(r+s)(\omega_p t - \kappa_p x)} \tag{8}$$

where $\kappa_{[r]} = \kappa + r\kappa_p$ and $\omega_{(r)} = \omega + r\omega_p$ are shorthand notations for wavenumber and frequency shifts, respectively, for any integer r. To exploit the orthogonality of harmonic functions, both sides of Eq. (8) are first multiplied by $\mathrm{e}^{-\mathrm{i}\ell(\omega_p t - \kappa_p x)}$, with ℓ being a dummy integer variable, to get

$$\sum_{r=-\infty}^{\infty}\sum_{s=-\infty}^{\infty} \kappa_{[r+s]}\kappa_{[s]} u_s E_r \mathrm{e}^{i(r+s-\ell)(\omega_p t - \kappa_p x)} = \sum_{r=-\infty}^{\infty}\sum_{s=-\infty}^{\infty} \omega_{(r+s)}\omega_{(s)} u_s \rho_r \mathrm{e}^{i(r+s-\ell)(\omega_p t - \kappa_p x)} \tag{9}$$

Following which, both sides of Eq. (9) are averaged over one spatial and temporal period as follows:

$$\frac{\omega_p}{2\pi}\frac{\kappa_p}{2\pi} \int_0^{\frac{2\pi}{\omega_p}} \int_0^{\frac{2\pi}{\kappa_p}} \sum_{r=-\infty}^{\infty}\sum_{s=-\infty}^{\infty} \big(\kappa_{[r+s]}\kappa_{[s]} E_r - \omega_{(r+s)}\omega_{(s)}\rho_r\big) u_s \mathrm{e}^{i(r+s-\ell)(\omega_p t - \kappa_p x)} dx\, dt = 0 \tag{10}$$

Given the orthogonality of harmonic functions, all the summation terms in the left hand side of Eq. (10) can be zeroed out, except for when $r+s=\ell$ (or equivalently, $r=\ell-s$). As such, Eq. (10) reduces to

$$\sum_{s=-\infty}^{\infty}\big(\kappa_{[r]}\kappa_{[s]}E_{r-s}-\omega_{(r)}\omega_{(s)}\rho_{r-s}\big)u_s=0 \tag{11}$$

Expanding the powers of ω gives

$$\sum_{s=-\infty}^{\infty}\big(\rho_{r-s}\omega^2+\rho_{r-s}(r+s)\omega_p\omega+\rho_{r-s}rs\omega_p^2-\kappa_{[+r]}\kappa_{[+s]}E_{r-s}\big)u_s=0 \tag{12}$$

The infinite series in Eq. (12) can be truncated by imposing a finite bound d and consequently casting into a familiar matrix eigenvalue problem of the following form:

$$(\mathbf{A}\,\omega^2+\mathbf{B}\,\omega+\mathbf{C})\,\tilde{\mathbf{u}}=\mathbf{0} \tag{13}$$

where $\tilde{\mathbf{u}}=\begin{bmatrix}\tilde{u}_{-d}, & \dots, & \tilde{u}_{-1}, & \tilde{u}_0, & \tilde{u}_1, & \dots, & \tilde{u}_d\end{bmatrix}^T$ is the eigenvector, and the entries of matrices **A**, **B** and **C** are given by

$$A_{s,r}=\mu_{r-s} \tag{14a}$$

$$B_{s,r}=(r+s)\omega_p\mu_{r-s} \tag{14b}$$

$$C_{s,r}=rs\omega_p^2\mu_{r-s}-\kappa_{[+r]}\kappa_{[+s]}c_o^2\gamma_{r-s} \tag{14c}$$

where $c_o^2=\frac{E_o}{\rho_o}$ and

$$\mu_{r-s}=\frac{\rho_{r-s}}{\rho_0}=\delta_{r-s} \tag{15a}$$

$$\gamma_{r-s}=\frac{E_{r-s}}{E_0}=\delta_{r-s}+\frac{\alpha}{2}(\delta_{r-s-1}+\delta_{r-s+1})+\frac{\beta}{2}(\delta_{r-s-1}-\delta_{r-s+1}) \tag{15b}$$

III. GENERALIZED MODULATION SCENARIOS

By applying the most general form of harmonic stiffness modulation (real and imaginary variations in both space and time) to derive the eigenvalue problem depicted in Eq. (13), we are able to start from the generalized case and simplify down to specific cases of interest, as will be shown in the following subsections. We will start by a couple of simple examples where the modulation is purely real and either space- or time-periodic to confirm and validate the current framework. Following which, we will proceed to uncharted scenarios which will reveal the intriguing physics of complexly modulated elastic systems ranging from symmetry to existence conditions of different types of dispersion gaps. In the following, $E_o=\rho_o=1$ and all the parameters are expressed in arbitrary units.

A. Case 1: $E(x,t)=E_o\left[1+\alpha\cos(-\kappa_p x)\right]$ and Case 2: $E(x,t)=E_o\left[1+\alpha\cos(\omega_p t)\right]$

The stiffness modulation profile represented by Case 1 describes a traditional phononic bar, albeit with a harmonically-varying modulus rather than discrete periodic impedance mismatches. The emergence and behavior of Bragg bandgaps in infinite [44–46] and finite [47–49] phononic systems have been thoroughly studied over the past two decades. The approach adopted here is a free-wave approach where a real wavenumber κ is fed into the dispersion relation to obtain the real and imaginary components of the output frequency ω. The left column of Fig. 1a pits the real and imaginary components of the eigenfrequency, $\Re(\omega)$ and $\Im(\omega)$, against the real wavenumber κ

for Case 1 with $\alpha = 0.7$, $\beta = 0$, $\kappa_p = 1$, and $\omega_p = 0$. The former shows the first five dispersion bands (in a color-coded order) and reveal the existence of a phononic bandgap (PBG) between the first and second bands, while the latter shows a zero imaginary component of frequency across the entire wavenumber space, confirming the expected lack of temporal attenuation/amplification in the non-dissipative time-invariant elastic medium. Most recently, the emergence of κ-gaps, a region in the wavenumber space where two bands coalesce with complex conjugate eigenfrequencies, has been reported in elastic structures with complex spatially-modulated stiffness profiles [17], as well as spatially uniform elastic structures with real time-modulated stiffness profiles [5].

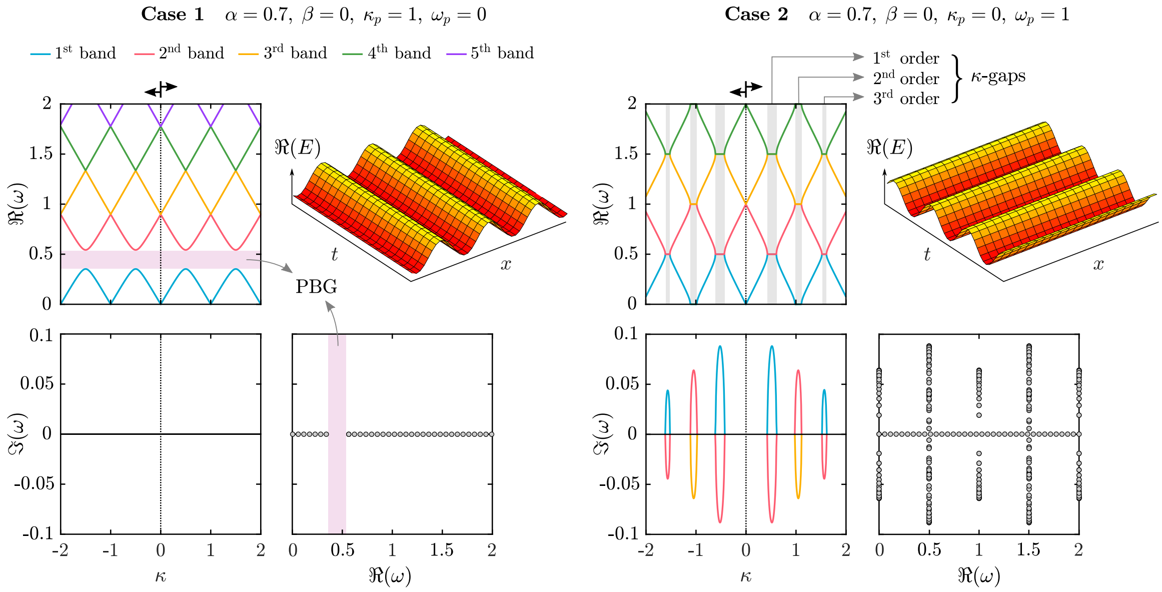

(a) **(b)**

FIG. 1. Dispersion analysis for the systems described by (a) Case 1: $\alpha = 0.7$, $\beta = 0$, $\kappa_p = 1$, and $\omega_p = 0$, and (b) Case 2: $\alpha = 0.7$, $\beta = 0$, $\kappa_p = 0$, and $\omega_p = 1$. The top left plot depicts the band structure, i.e., the real frequency $\Re(\omega)$ versus the wavenumber κ for each case. The bottom left and bottom right plots provide the variation of the imaginary frequency $\Im(\omega)$ versus κ and $\Re(\omega)$, respectively, for each case. A graphical representation of the real elastic modulus modulation $\Re(E)$ in space and time is provided in the top right corner of each case ($E_o = \rho_o = 1$).

Figure 1b shows Case 2 with $\alpha = 0.7$, $\beta = 0$, $\kappa_p = 0$, and $\omega_p = 1$. By inspecting Eqs. (13) through (15), it can be deduced that the **A**, **B** and **C** matrices are both real and symmetric in Case 2. Due to the properties of quadratic eigenvalue problems, eigenvalues of such a system can be either real values or complex conjugates [50]. As a result, we witness the formation of several κ-gaps as shown in the top left panel of Fig. 1b. These κ-gaps can be classified as κ-gaps of the n^{th} order, and sorted based on their proximity to the $\kappa = 0$ axis. Henceforth, we refer to the κ-gaps closest to the $\kappa = 0$ axis as 1^{st} order gaps. These 1^{st} order gaps form at the interface between the first and second, third and fourth, fifth and sixth bands, etc. We will refer to following set of κ-gaps as 2^{nd} order gaps. These are the first set of gaps that form at the interface between the second and third, fourth and fifth, fifth and sixth bands, etc, and so forth. The formation of κ-gaps corresponds to the onset of temporal amplification (or attenuation) regions captured by the positive (or negative) imaginary component of the eigenfrequency, $\Im(\omega)$ (bottom left panel of Fig. 1b). It can be seen that both the width (w.r.t. the wavenumber axis) and the amplification/attenuation level, i.e., $|\Im(\omega)|$, of the κ-gaps decrease as they move further away from $\kappa = 0$ and their order increases. It can also be seen κ-gaps of the same order that span the same wavenumber range but occur at different frequencies, have identical amplification/attenuation levels. As a result, $\Im(\omega)$ corresponding to the 1^{st} order κ-gap at the interface between the first and second dispersion bands lies on top of the 1^{st} order κ-gap between the third and fourth bands.

The bottom right panel of Fig. 1b plots the imaginary component of each eigenfrequency as a function of its real component, and confirms the presence of several complex conjugate eigenfrequencies which share the same real value but different imaginary parts at each κ-gap. The figure also reveals that even-ordered κ-gaps correspond to $\Re(\omega) = \vartheta/2$ for $\vartheta \in \{0, 2, 4, \dots\}$, while odd-ordered κ-gaps correspond to $\Re(\omega) = \varphi/2$ for $\varphi \in \{1, 3, 5, \dots\}$. Finally, the frequency of each κ-gap is identical for left- and right-going waves, and the symmetry of the $\Re(\omega)$-κ plot about the $\kappa = 0$ axis is preserved.

B. Cases 3 and 4: $E(x,t) = E_o\left[1 + \alpha\cos(\omega_p t - \kappa_p x)\right]$ for $\nu < 1$ and $\nu > 1$, respectively

For an elastic bar with a spatiotemporally modulated stiffness, we define the modulation speed v_p as the ratio between the temporal modulation frequency ω_p and the spatial modulation frequency κ_p, and the modulation speed ratio as $\nu = v_p/c_o$, where c_o denotes the sonic speed in the medium. Figure 2a shows a phononic bar with a purely real space-time-periodic elastic modulus, i.e., Case 3, with $\alpha = 0.7$, $\beta = 0$, $\kappa_p = 1$, and $\omega_p = 0.2$. The previous parameters amount to a sub-sonic modulation speed ($\nu < 1$) which give rise to a direction-dependent PBG, i.e., a bandgap which spans different frequencies for positive and negative values of κ [9], a behavior which has been recently exploited to realize nonreciprocal wave transmission or a diode-like behavior in elastic metamaterials [11]. As the value of ν increases, the modulation speed approaches that of the wave. The $\nu = 1$ condition denotes what is referred to as a *luminal* modulation in photonics [51]. Further details about the implications of this condition can be found in the work of Cassedy and Oliner [52] and Cassedy [53]. The dispersive behavior of the medium drastically changes beyond that point, once ν exceeds unity, as demonstrated by Case 4.

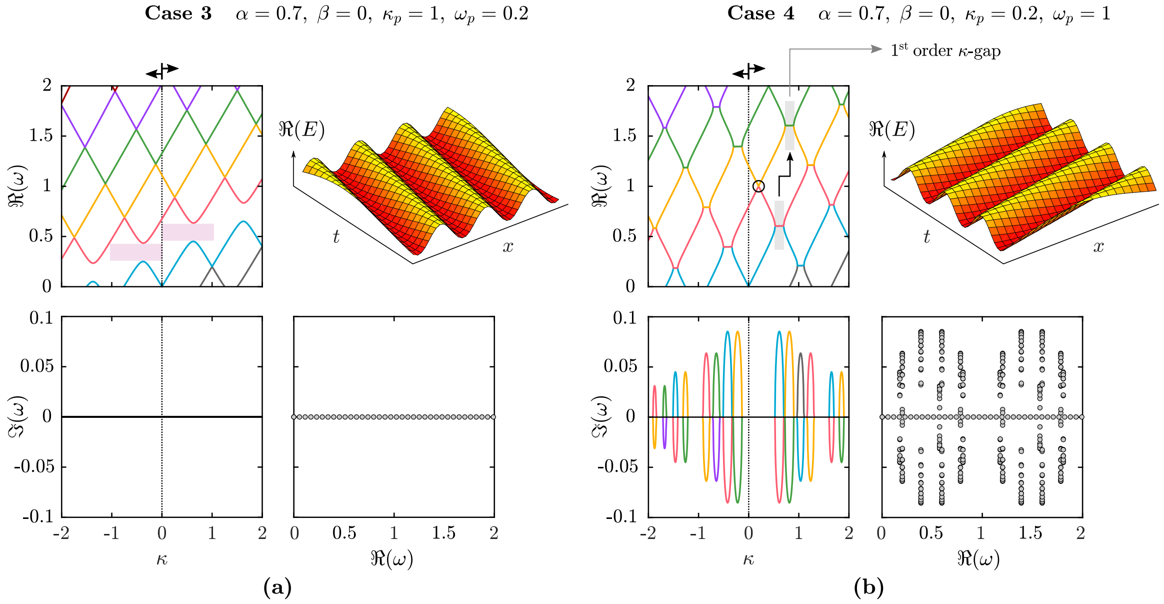

(a) (b)

FIG. 2. Dispersion analysis for the systems described by (a) Case 3: $\alpha = 0.7$, $\beta = 0$, $\kappa_p = 1$, and $\omega_p = 0.2$, and (b) Case 4: $\alpha = 0.7$, $\beta = 0$, $\kappa_p = 0.2$, and $\omega_p = 1$. The top left plot depicts the band structure, i.e., the real frequency $\Re(\omega)$ versus the wavenumber κ for each case. The bottom left and bottom right plots provide the variation of the imaginary frequency $\Im(\omega)$ versus κ and $\Re(\omega)$, respectively, for each case. A graphical representation of the real elastic modulus modulation $\Re(E)$ in space and time is provided in the top right corner of each case ($E_o = \rho_o = 1$).

In Case 4, the parameters $\alpha = 0.7$, $\beta = 0$, $\kappa_p = 0.2$, and $\omega_p = 1$ lead to a super-sonic modulation speed ($\nu > 1$). As a result, κ-gaps which are asymmetric with respect to the $\kappa = 0$ axis are generated as can be seen in Fig. 2b. These κ-gaps are not only asymmetric with respect to the wavenumber axis, but also the frequencies they correspond to differ for left- and right-going waves, indicating a nonreciprocal wave amplification/attenuation capability. It is important to point out that the symmetry breakage of the band structure, and the overall tilting associated with it, slightly alters the location of κ-gaps of the same order which now no longer span the same range of κ values. For visualization, this is graphically pointed out in the horizontal shift between the lower-frequency and the higher-frequency 1st order κ-gaps in the $\Re(\omega)$-κ plot of Fig. 2b. As a result, while these two κ-gaps no longer share the same proximity to the $\kappa = 0$ axis, we still define both of them as 1st order κ-gaps since they are the closest gaps to the $\kappa = 0$ axis that take place at the interface between the first and second bands, and the third and fourth, respectively. (The same definition extends to the κ-gaps observed in the band structures of Cases 7 and 8 which also exhibit tilting). The circled region in the same figure denotes the shifted location of the meeting point between the second and third bands, which has deviated from the $\kappa = 0$ axis. Finally, similar to Case 2, we note that both the width (w.r.t. the wavenumber axis) and the amplification/attenuation level, i.e., $|\Im(\omega)|$, of the κ-gaps become smaller for higher order gaps. In other words, they gradually shrink and eventually vanish as we move further away from the $\kappa = 0$ axis.

C. Case 5: $E(x,t) = E_o\left[1 + \mathrm{i}\beta\sin(-\kappa_p x)\right]$ and Case 6: $E(x,t) = E_o\left[1 + \mathrm{i}\beta\sin(\omega_p t)\right]$

In Cases 5 and 6, we examine a phononic bar with a stiffness modulation profile which includes a purely imaginary spatial modulation term and a purely imaginary temporal modulation term, respectively. In both of these cases, we utilize an odd function, namely sin(•), to synthesize a gain-loss mechanism and trigger periodic energy pumping into and out of the system, akin to non-Hermitian modulations of optical systems [38]. A close inspection of Eq. (13) for Case 5 reveals a suppression of the matrix **B** due the fact that $\omega_p = 0$. Consequently, Eq. (13) becomes a linear eigenvalue problem. Furthermore, it can be observed that while both **A** and **C** are real, only **A** is symmetric. The role of β in breaking the symmetry of **C** becomes evident, as it converts a conventional Hermitian system to a non-Hermitian (cyclic) system, in which **C** is a summation of Hermitian and skew-Hermitian matrices. Figure 3a depicts Case 5 with $\alpha = 0$, $\beta = 0.7$, $\kappa_p = 1$, and $\omega_p = 0$. Despite the presence of a spatial modulation, we notice the absence of any PBGs when such modulation is purely imaginary. And despite the absence of a temporal modulation, the structure exhibits some κ-gaps. In this scenario, four observations can be made about the emerging κ-gaps, all of which are notably distinct from the behavior of κ-gaps obtained via real temporal (Case 2) or real spatiotemporal (Case 4) modulations:

1. The $\Re(\omega)$-κ plot shows that κ-gaps only form at a single frequency ($\omega = 0.5$).
2. The $\Re(\omega)$-κ plot also shows that all even-ordered κ-gaps cease to exist.
3. The $\Im(\omega)$-κ plot shows that peak amplification/attenuation levels associated with the κ-gaps, i.e., $\pm|\Im(\omega)|$, do not increase for higher order gaps as we move further away from the $\kappa = 0$ axis, and instead remain constant.
4. Both the $\Re(\omega)$-κ and $\Im(\omega)$-κ plots show that the width of the κ-gaps remains constant as we move further away from the $\kappa = 0$ axis.

Figure 3b represents Case 6 with $\alpha = 0$, $\beta = 0.7$, $\kappa_p = 0$, and $\omega_p = 1$. Here, a simultaneous combination of PBGs and even-ordered κ-gaps take place. Additionally, it is observed that the PBGs and κ-gaps take turns and are alternating in nature, with only one of the two happening between each two consecutive dispersion bands. The bottom right panel of Fig. 3b confirms that the κ-gaps correspond to $\Re(\omega) = \vartheta/2$ for $\vartheta \in \{0, 2, 4, \dots\}$, and the bottom left panel shows that contrary to Fig. 3a, their peak amplification/attenuation levels decrease as we move further away from the $\kappa = 0$ axis towards higher order κ-gaps. The emergence of PBGs in Case 6 is especially noteworthy given the lack of a spatial modulus variation which is typically a hallmark feature of structures with Bragg bandgaps. Interestingly, the behavior of these PBGs mimics that of the κ-gaps in Case 2, where the same temporal modulation of the elastic modulus was imposed as a real term. Namely, the frequency range of the PBGs shrinks as we move further from the $\kappa = 0$ axis until the gap eventually closes. Figure 4a provides the dispersion diagram of Case 6 with an extended wavenumber-axis range, and the adjacent close-up inset confirms the gradual narrowing of the space between the two dispersion branches flanking the PBG as $|\kappa|$ increases. PBG bounds obtained by tracing the edges of these two branches are shown in Fig. 4b. To illustrate the manifestation of such PBGs which vary with the wavenumber, a finite bar consisting of 50 unit cells (i.e., modulation cycles) is excited at its midpoint via two different frequencies, namely $\Re(\omega) = 0.48$ (Sim I) and 0.42 (Sim II). The two simulations are also indicated on the close-up inset of Fig. 4a where it can be seen that Sim I lies within the space of the PBG for low values of κ and doesn't hit the lowest dispersion branch until $\kappa = 2.5$, marked as point D. On the other hand, owing to its excitation frequency, Sim II is unable to evade the same dispersion branch and intersects with it at the locations marked A, B, and C. The full wavenumber spectrum of both simulations is shown in Figs. 4c and d, and shows the implication of this behavior on the finite structural response. The highest peak in both plots takes place at the same κ value which corresponds to (and is caused by) the modulation frequency of $\omega_p = 1$. Aside from this peak, the bar's response in Sim I in Fig. 4c is insignificant albeit for the κ value at point D, whereas contributions from wavenumbers at locations A, B, and C can be clearly seen in the bar's response in Sim II, shown in Fig. 4d; both observations being very consistent with Figs. 4a. Contributions from higher wavenumbers (i.e., $\kappa > 3$) were found to be negligible in both cases. As a final confirmation, the insets in Figs. 4c and d show a single snapshot of the spatial wave propagation of both excitations in the finite bar following a low-pass filter (LPF) only admitting the $\kappa < 0.75$ portion of the wavenumber spectrum. The Sim II inset in Fig. 4d shows the unimpeded propagation of the wave in the finite medium consistent with the lack of a PBG at location A, while that in Fig. 4c shows an insignificant response since the excitation frequency of Sim I squarely falls inside the PBG in the $\kappa < 0.75$ range.

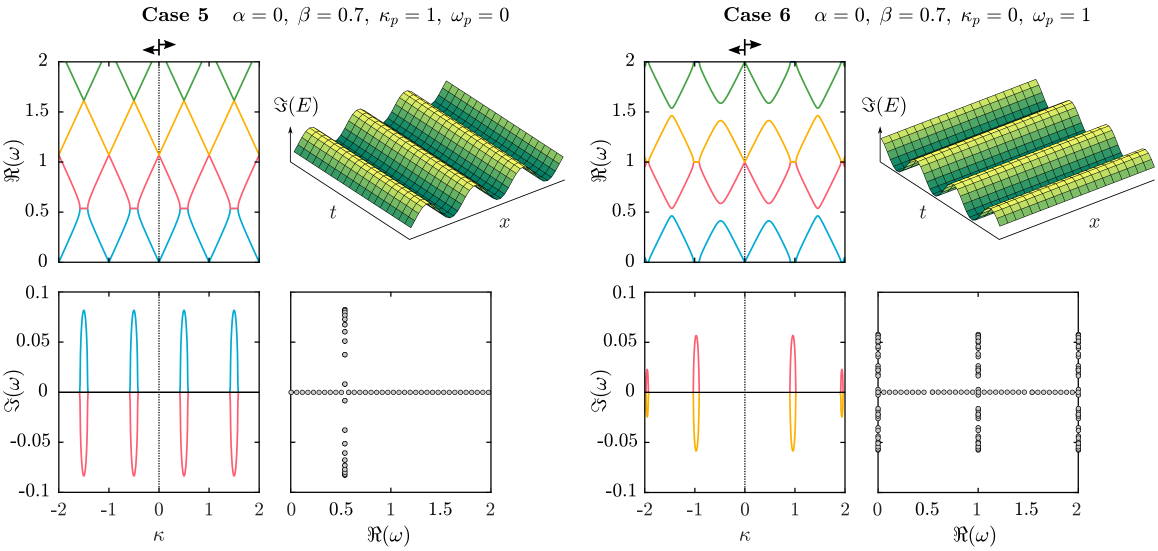

(a) **(b)**

FIG. 3. Dispersion analysis for the systems described by (a) Case 5: $\alpha = 0$, $\beta = 0.7$, $\kappa_p = 1$, and $\omega_p = 0$, and (b) Case 6: $\alpha = 0$, $\beta = 0.7$, $\kappa_p = 0$, and $\omega_p = 1$. The top left plot depicts the band structure, i.e., the real frequency $\Re(\omega)$ versus the wavenumber κ for each case. The bottom left and bottom right plots provide the variation of the imaginary frequency $\Im(\omega)$ versus κ and $\Re(\omega)$, respectively, for each case. A graphical representation of the imaginary elastic modulus modulation $\Im(E)$ in space and time is provided in the top right corner of each case ($E_o = \rho_o = 1$).

D. Cases 7 and 8: $E(x,t) = E_o\left[1 + \mathrm{i}\beta\sin(\omega_p t - \kappa_p x)\right]$ for $\nu < 1$ and $\nu > 1$, respectively

The last two scenarios combine the imaginary spatial and temporal modulations investigated in Cases 5 and 6 in one term to capture the behavior of a phononic bar with a purely imaginary space-time-periodic elastic modulus profile. Analogous to Cases 3 and 4, we investigate the behavior of this structure at sub-sonic ($\nu < 1$, Case 7) and super-sonic ($\nu > 1$, Case 8) modulation speeds. The parameters for Case 7 are: $\alpha = 0$, $\beta = 0.7$, $\kappa_p = 1$, and $\omega_p = 0.2$. The system in this scenario shares select features from Cases 4 (real space-time-periodic) and 5 (imaginary space-periodic) and represents a hybrid combination thereof. Similar to Case 4, Case 7 exhibits asymmetric κ-gaps, both with respect to the $\kappa = 0$ axis and with respect to the frequency $\Re(\omega)$ at which they occur for left- and right-going waves. However, similar to Case 5, we observe: (1) a lack of even-ordered κ-gaps, (2) a constant level of amplification/attenuation, $\Im(\omega)$, for all κ-gaps, and (3) a constant width or κ range spanned by all the κ-gaps regardless of order.

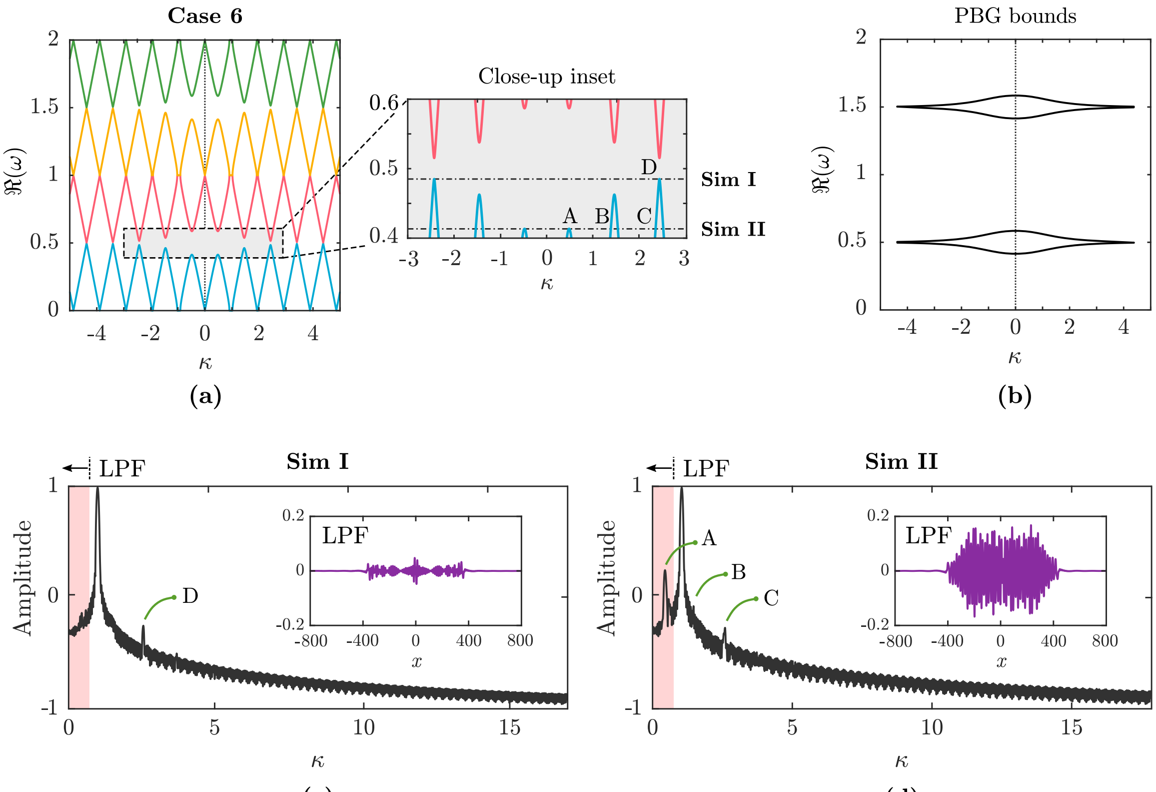

(a) (b)

(c) (d)

FIG. 4. (a) Dispersion diagram of Case 6 with an extended wavenumber axis. Close-up inset shows the gradually narrowing bandgap region and indicates the excitation frequencies for two simulations labeled Sim I and Sim II. (b) Bounds of the two PBGs forming between the first and second bands and between the third and forth bands. PBGs shrink at increasing distance from the $\kappa = 0$ axis and eventually close. (c-d) Wavenumber spectrum (i.e., spatial FFT) of the response of a finite-sized bar made of 50 unit cells to a midpoint excitation at a frequency of: (c) $\Re(\omega) = 0.48$ (Sim I) and (d) $\Re(\omega) = 0.42$ (Sim II). Markers at A, B, C, and D confirm peaks corresponding to the dispersion crossings shown in the close-up inset of (a). Insets in (c) and (d) display snapshots of the spatial wave propagation in the finite bar following a low-pass filter (LPF) admitting the $\kappa < 0.75$ portion, or the shaded region, of the wavenumber spectrum.

Figure 5b provides the behavior of Case 8 with $\alpha = 0$, $\beta = 0.7$, $\kappa_p = 0.2$, and $\omega_p = 1$, which represents a super-sonic modulation ($\nu > 1$) of the imaginary space-time-periodic stiffness profile. The system in this case largely behaves in a manner similar to Case 6, but with a nonreciprocal tilt of the overall band structure as expected. Specifically, we observe the absence of all odd-ordered κ-gaps as well as an alternating cycle of nonreciprocal PBGs and even-ordered κ-gaps as we move up the real frequency axis. The width of the even-ordered κ-gaps narrows down for higher order gaps. Additionally, also similar to Case 6, the frequency range of the PBGs also shrinks as we move further from the $\kappa = 0$ axis until the gap eventually closes.

As a final note, it should be pointed out that since eigenfrequencies inside κ-gaps are represented by complex conjugates, the amplification and attenuation levels for a specific κ-gap will remain identical for all and any cases.

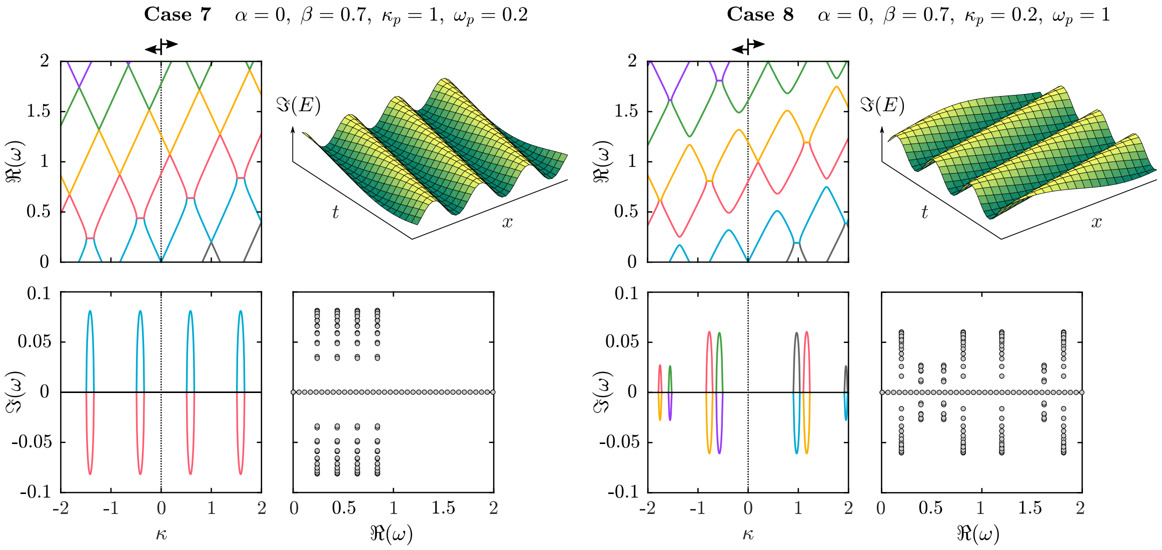

(a) **(b)**

FIG. 5. Dispersion analysis for the systems described by (a) Case 7: $\alpha = 0$, $\beta = 0.7$, $\kappa_p = 1$, and $\omega_p = 0.2$, and (b) Case 8: $\alpha = 0$, $\beta = 0.7$, $\kappa_p = 0.2$, and $\omega_p = 1$. The top left plot depicts the band structure, i.e., the real frequency $\Re(\omega)$ versus the wavenumber κ for each case. The bottom left and bottom right plots provide the variation of the imaginary frequency $\Im(\omega)$ versus κ and $\Re(\omega)$, respectively, for each case. A graphical representation of the imaginary elastic modulus modulation $\Im(E)$ in space and time is provided in the top right corner of each case ($E_o = \rho_o = 1$).

E. Verification of κ-gaps and recovery of imaginary eigenfrequency component of a finite stiffness-modulated system

The formation of κ-gaps and the accompanying amplification/attenuation regions in the $\Im(\omega)$-κ data presented so far have been predicted using an infinite system approach, which adopts the Floquet theorem augmented with a plane wave expansion (PWE) method, as outlined in Section II. As a result, it is incumbent upon us to examine and verify the onset of such amplification/attenuation regimes in finite realizations of such stiffness-modulated systems. For brevity, we focus here on Cases 1 and 5 which represent real and imaginary spatial modulations of the time-invariant elastic modulus of a one-dimensional phononic bar. To verify the imaginary component of the eigenfrequencies, $\Im(\omega)$, using the finite element method (FEM), we consider a finite bar of 50 unit cells where each cell spans one full cycle of the spatial modulation of the elastic modulus E and is discretized using 30 finite elements, as depicted in Fig. 6a. As a result, the finite structure contains a total of $50 \times 30 = 1,500$ finite elements which are modeled using conventional 2-noded 1D bar elements and are assembled to form the equation of motion of the entire structure. The eigenfrequencies are obtained from the free vibration eigenvalue problem $[\mathbf{M}^{-1}\mathbf{K}]\mathbf{u} = \omega^2\mathbf{u}$, where $\mathbf{u}$ is the discretized displacement field vector, and $\mathbf{M}$ and $\mathbf{K}$ are the overall mass and stiffness matrices, respectively. The resultant eigenfrequencies are split into $\Re(\omega)$ and $\Im(\omega)$ which are plotted in the top and bottom panels of Figs. 6b and c, representing close-up regions of Figs. 1a and 3a. It should be noted that the value of κ corresponding to each eigenfrequency is computed from a spatial Fourier transform of the corresponding displacement field of the 1500-elements structure. An excellent agreement can be seen between the infinite dispersion bands obtained for both cases and the discrete frequency-wavenumber obtained from the finite structures representing both cases, including the κ-gap regions of Case 5. More importantly, the bottom panel of Figs. 6b and c, verifies the amplification/attenuation levels, i.e., $\Im(\omega)$, corresponding to the κ-gaps of Case 5, in addition to confirming the lack of such gaps in Case 1 throughout the entire κ-space.

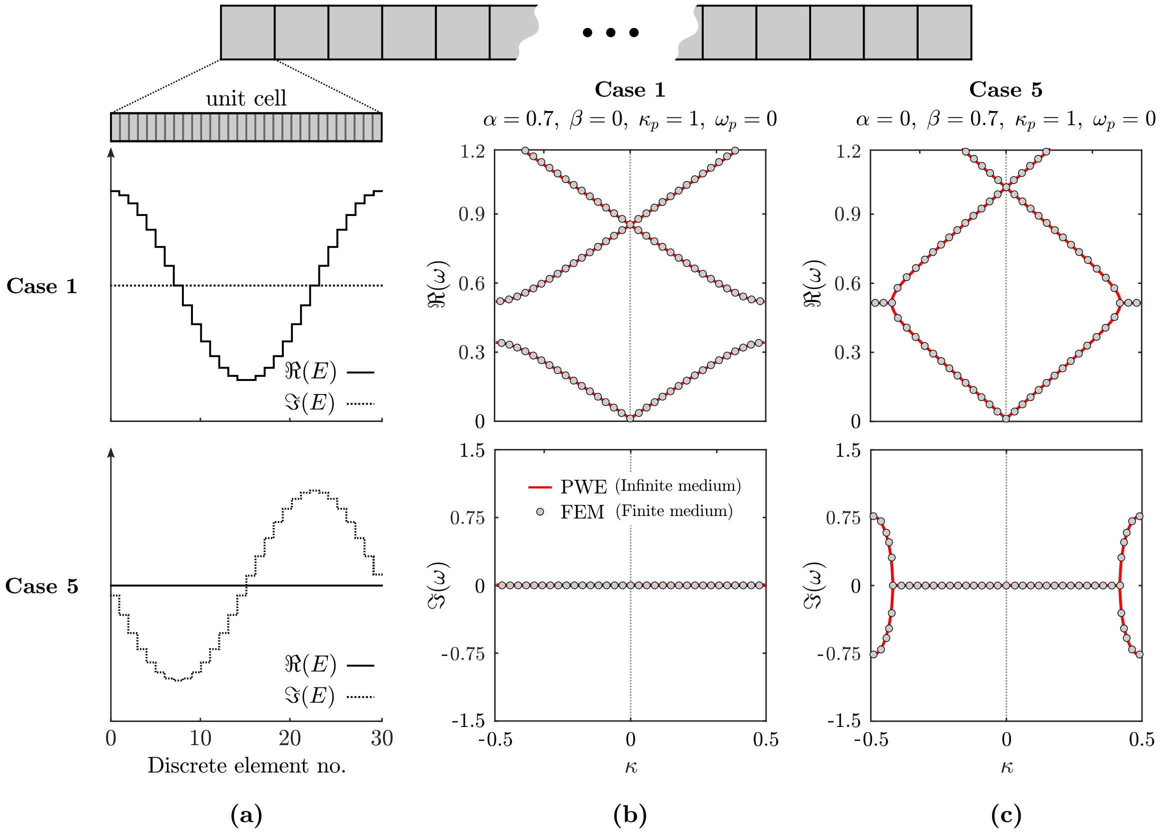

FIG. 6. Discrete dispersion data obtained from finite realizations of Case 1: $\alpha = 0.7$, $\beta = 0$, $\kappa_p = 1$, and $\omega_p = 0$, and Case 5: $\alpha = 0$, $\beta = 0.7$, $\kappa_p = 1$, and $\omega_p = 0$. (a) Discretized elastic modulus profile over a single spatial modulation cycle spanning a unit cell of 30 finite elements for Case 1 (top) and Case 5 (bottom). (b-c) $\Re(\omega)$-κ and $\Im(\omega)$-κ diagrams for Case 1 (left) and Case 5 (right). Finite structure eigenfrequencies (via FEM) are denoted by circle markers and infinite band structure (via PWE) is denoted by solid lines.

IV. CONDITIONS FOR DIRECTIONAL AMPLIFICATION

Beyond the eight distinct modulation categories represented by Cases 1 through 8, any other form of stiffness modulation can be written as a combination of these cases, and the behavior resulting therefrom will generally depend on two primary factors, the first is whether the absolute value of the ratio β/α is less than, greater than, or equal to 1, and the second is whether the modulation speed ratio ν is less than, greater than, or equal to 1. Let us consider sufficiently weak interactions, which enable first-order harmonics to make accurate representations of the system at hand. As a result, we truncate the infinite matrices of Eq. (14) by setting $d = 1$. This leads to a homogeneous set of equations governing the free vibrations of a dynamic system with three coupled harmonic oscillators, that are described by

$$\left(\mathbf{A}_{\lfloor d=1 \rfloor}\,\omega^2 + \mathbf{B}_{\lfloor d=1 \rfloor}\,\omega + \mathbf{C}_{\lfloor d=1 \rfloor}\right)\tilde{\mathbf{u}}_{\lfloor d=1 \rfloor} = \mathbf{0} \tag{16}$$

where $\tilde{\mathbf{u}}_{\lfloor d=1 \rfloor} = \begin{bmatrix}\tilde{u}_{-1} & \tilde{u}_0 & \tilde{u}_1\end{bmatrix}^T$, and

$$\mathbf{A}_{\lfloor d=1 \rfloor} = \begin{bmatrix}1 & 0 & 0\\ 0 & 1 & 0\\ 0 & 0 & 1\end{bmatrix} \tag{17a}$$

$$\mathbf{B}_{\lfloor d=1 \rfloor} = \begin{bmatrix} -2\omega_p & 0 & 0 \\ 0 & 0 & 0 \\ 0 & 0 & 2\omega_p \end{bmatrix} \tag{17b}$$

$$\mathbf{C}_{\lfloor d=1 \rfloor} = \begin{bmatrix} \omega_p^2 - c_o^2(\kappa - \kappa_p)^2 & -c_o^2\kappa(\kappa - \kappa_p)\frac{\alpha+\beta}{2} & 0 \\ -c_o^2\kappa(\kappa - \kappa_p)\frac{\alpha-\beta}{2} & -c_o^2\kappa^2 & -c_o^2\kappa(\kappa + \kappa_p)\frac{\alpha+\beta}{2} \\ 0 & -c_o^2\kappa(\kappa + \kappa_p)\frac{\alpha-\beta}{2} & \omega_p^2 - c_o^2(\kappa + \kappa_p)^2 \end{bmatrix} \tag{17c}$$

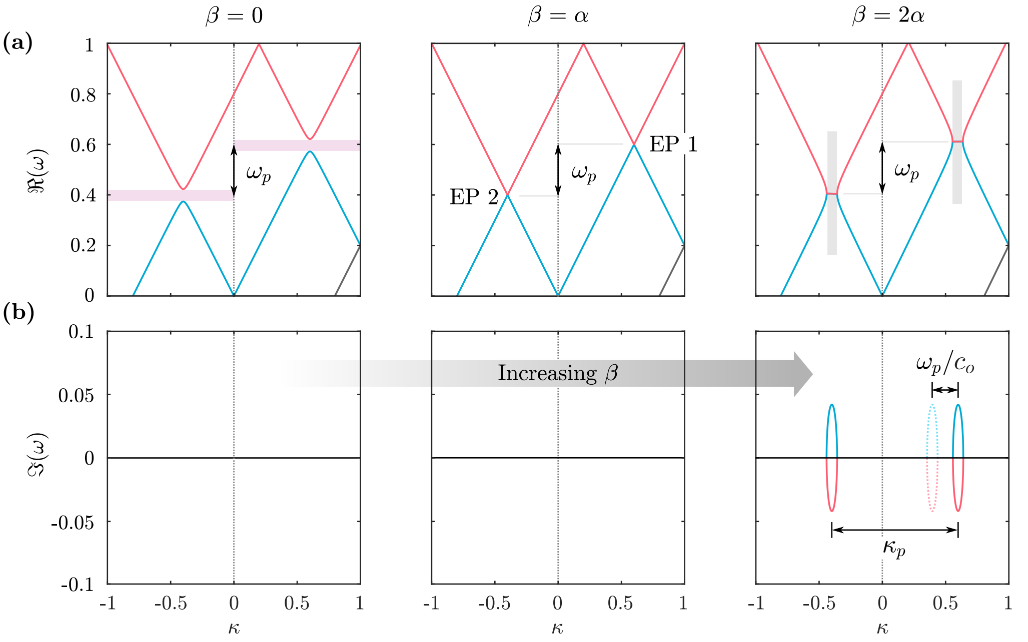

FIG. 7. Transition from PBGs to κ-gaps past the $\beta = \alpha$ threshold. (a) $\Re(\omega)$-κ diagrams and (b) $\Im(\omega)$-κ diagrams for $\beta = 0$ (left), $\beta = \alpha$ (middle) and $\beta = 2\alpha$ (right). System parameters used are: $\alpha = 0.2$, $\kappa_p = 1$, $\omega_p = 0.2$, and $E_o = \rho_o = 1$. Vertical and horizontal shifts culminating from band tilting are marked as functions of temporal modulation frequency ω_p, spatial modulation frequency κ_p, and sonic speed c_o.

Figures 7a and b show the $\Re(\omega)$-κ and $\Im(\omega)$-κ plots of three systems, respectively, corresponding to $\beta = 0$, $\beta < \alpha$, and $\beta > \alpha$. In the three cases, $\alpha = 0.2$ was chosen to keep the interactions weak and a modulation frequency of $\omega_p = 0.2$ was used to break the system's reciprocity. The transition from PBGs ($\beta = 0$) to κ-gaps ($\beta = 2\alpha$) is obvious and a band structure tilt equal to the value of ω_p can be observed across all three plots of Fig. 7a. In the leftmost plot, the tilt represents the frequency shift between the PBGs associated with forward and backward waves. In the middle plot, it represents the frequency shift between the two exceptional points, labeled as EP 1 and EP 2. In the rightmost plot, it represents the frequency shift between the κ-gaps associated with forward and backward waves. In addition to the vertical frequency shift, it is important to note that the emergent κ-gaps in the $\beta = 2\alpha$ scenario are also asymmetric with respect to $\kappa = 0$ line and, consequently, exhibit a horizontal shift which can be interestingly quantified in two ways. The small shift between the right κ-gap and the reflected version of the left κ-gap (shown via faded colors) is equal to ω_p/c_o, while the overall horizontal distance between the two κ-gaps is equal to the spatial modulation κ_p.

Figure 8 shows the evolution of the dispersion behaviour of the system as the ratio β/α varies between -2 and 2. Of interest is the case where $\beta = \alpha$, and $\mathbf{C}_{\lfloor d=1 \rfloor}$ simplifies to

$$\mathbf{C}_{\lfloor d=1 \rfloor}\Big|_{\beta=\alpha} = \begin{bmatrix} \omega_p^2 - c_o^2(\kappa - \kappa_p)^2 & -c_o^2\kappa(\kappa - \kappa_p)\alpha & 0 \\ 0 & -c_o^2\kappa^2 & -c_o^2\kappa(\kappa + \kappa_p)\alpha \\ 0 & 0 & \omega_p^2 - c_o^2(\kappa + \kappa_p)^2 \end{bmatrix} \tag{18}$$

For a certain set of κ values, the matrix given by Eq. (18) becomes a defective stiffness matrix which cannot be diagonalized. In such case, the corresponding system would not support a complete basis of eigenvectors and its algebraic multiplicity exceeds its geometric multiplicity. This phenomena is attributed to exceptional points in the parameter space which, in this problem, appear at the $|\beta/\alpha| = 1$ point for κ values at the boundaries of the Brillouin zone. As shown in the top panel of Figs. 8c and d, the eigenvalues of the system coalesce at this point and become complex conjugates beyond it. The bottom panel of Figs. 8c and d show that the two eigenvectors, represented by $\tilde{\mathbf{u}}_{\lfloor d=1 \rfloor}$, become perfectly identical at the same point, which is verified by their difference being zero for any $|\beta/\alpha| \geq 1$, further confirming that the dynamics of the system significantly change before and after each exceptional point.

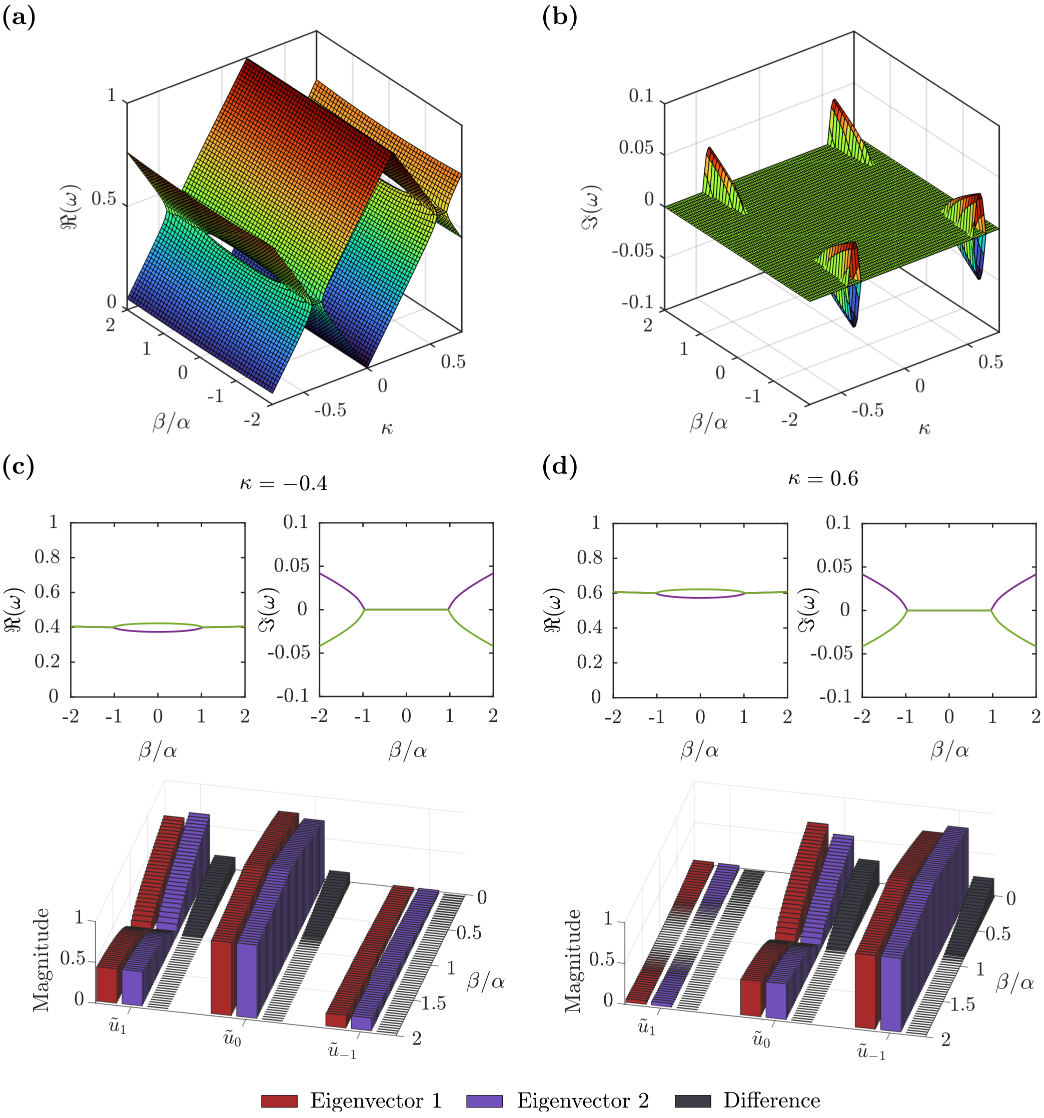

FIG. 8. Effect of β/α on the dispersion behavior, κ-gaps, and exceptional points. (a) $\Re(\omega)$-κ and (b) $\Im(\omega)$-κ relations for different β/α values. Exceptional points can be observed at $|\beta/\alpha| = 1$. (c-d) Coalescence of eigenvalues (top panel) and eigenvectors (bottom panel) for (c) $\kappa = -0.4$ and (d) $\kappa = 0.6$. Components of the first and second eigenvectors are different for any $\beta/\alpha < 1$ and identical for $\beta/\alpha \geq 1$, as confirmed by the difference bar in both (c) and (d). System parameters used: $\alpha = 0.2$, $\kappa_p = 1$, $\omega_p = 0.2$, and $E_o = \rho_o = 1$.

Next, we investigate the amplification behavior associated with exceptional points at $|\beta/\alpha| = 1$ in the presence and absence of a temporal modulation. The solid lines in Fig. 9a and b show the system's dispersion bands when $\beta/\alpha = \pm 1$ in the absence of a temporal modulation, i.e., $\omega_p = 0$. The bands are color-coded in the same way they've been throughout this paper, and the two exceptional points, EP 1 and EP 2, are indicated on the figure. In this case, EP 1 and EP 2 are symmetric with respect to the $\kappa = 0$ axis and share the same frequency, $\omega_{\text{EP}} = 0.5$. The dashed lines in the same figure show the transition of the dispersion diagram from $\beta/\alpha < 1$ to $\beta/\alpha > 1$, namely the changeover from PBGs to κ-gaps. Figure 9c shows the same set of dispersion lines but when a temporal modulation of $\omega_p = 0.2$ is introduced. Finally, Fig. 9d shows the behavior of the system when $\beta/\alpha = -1$ and $\omega_p = 0.2$. Owing to the value of ω_p, EP 1 and EP 2 in both Figs. 9c and d take place at $\omega_{\text{EP}} = 0.6$ and $\omega_{\text{EP}} = 0.4$, respectively. Figures 9e through p show the numerically reconstructed dispersion surfaces which are obtained using the "General Form PDE" module of COMSOL Multiphysics, with Eq. (1) being directly used to formulate the model. The geometry is constructed using 2000 discrete points along a 1D array with a resolution of 10 points per wavelength, and a zero flux boundary condition is applied to both ends. A Gaussian excitation of the form $f(t) = e^{(t_0-t)^2/2\sigma}\sin(\omega_i t)$ is applied using the flux/source boundary condition at the middle of the model and 2D FFTs are performed on the time-domain fields to obtain the dispersion data. For the wideband excitations, the following excitation parameters are chosen: $\sigma = 1$, $t_0 = 20$, and $\omega_i = 0.5$. To impose narrowband excitations, σ is set to 40 and ω_i is tuned to the center frequency of interest, as indicated on the individual figures. For convenience, the shape of the exciting waveform is plotted alongside each simulation. To avoid reflections, the simulations are only performed up to the time required for the waves to reach the boundaries.

By inspecting the wideband excitation cases in Figs. 9e-h, significant amplification can be observed in each of the four cases at one of the two aforementioned EPs. The sign of the β/α ratio dictates which EP becomes amplified. The amplification of EP 1 corresponds to $\beta/\alpha = +1$ (e.g., Figs. 9e and g) while the amplification of EP 2 corresponds to $\beta/\alpha = -1$ (e.g., Fig. 9f and h). We will henceforth refer to the the frequency of the amplified EP as $\omega_{\text{EP/amp}}$. To further investigate the behavior of these EPs, a narrowband excitation targeting the frequency of the amplified EP, i.e., $\omega_i = \omega_{\text{EP/amp}}$, is applied to each of the four cases. In the absence of ω_p, the narrowband excitations in Fig. 9i and j generate the same amplification as that of the wideband excitations shown in Fig. 9e and f, respectively. However, in the presence of a temporal modulation of $\omega_p = 0.2$, neither one of the narrowband excitations used in Figs. 9k and l is able to generate the same amplification achieved by their respective wideband excitations in Figs. 9g and h. Given the influence of temporal modulation on the underlying system dynamics, exciting the structure at different up- and down-harmonics of the amplified EP frequency becomes relevant [54]. To this end, a narrowband excitation corresponding to $\omega_i = \omega_{\text{EP/amp}} + \omega_p$ is imposed in Figs. 9m and n, and a narrowband excitation corresponding to $\omega_i = \omega_{\text{EP/amp}} - \omega_p$ is imposed in Figs. 9o and p. The results show that no amplification takes place in either Fig. 9m and p, but does take place in both Fig. 9o and n at the same EP that was shown to be amplifiable using a wideband excitation. As such, the following conclusions can be made:

1. In the absence of a temporal modulation (i.e., $\omega_p = 0$), both wide and narrowband excitations with $\omega_i = \omega_{\text{EP}}$ will trigger an amplification at the EP's whose location has the same sign for κ and β/α. In here, EP 1 is amplified when $\beta/\alpha = +1$ while EP 2 is amplified when $\beta/\alpha = -1$.
2. In the presence of a temporal modulation (i.e., $\omega_p \neq 0$):
    (a) A wideband excitation will result in amplification at a single EP location, $\omega_{\text{EP/amp}}$. However, a narrowband excitation of $\omega_i = \omega_{\text{EP/amp}}$ will fail to reproduce such amplification.
    (b) For $\beta/\alpha = \pm 1$ and an amplifiable EP at $\omega_{\text{EP/amp}}$, a narrowband excitation of $\omega_i = \omega_{\text{EP/amp}} \mp \omega_p$ is needed to activate the EP amplification.

To further elaborate, consider the analysis presented in Fig. 10 where different components of the first eigenvector are plotted for several scenarios, all sharing the following feature: $|\beta| = |\alpha|$. In Fig. 10a, where $\beta/\alpha = +1$, a noticeable drop in the amplitude of $\tilde{u}_0$ is observed at $\kappa = 0.6$. Leading up to the same value of κ, a rise in the amplitude of $\tilde{u}_{-1}$ can also be observed. This is indicative of an amplification taking place at EP 1 (here at $\kappa = 0.6$) corresponding to $\beta/\alpha = +1$,

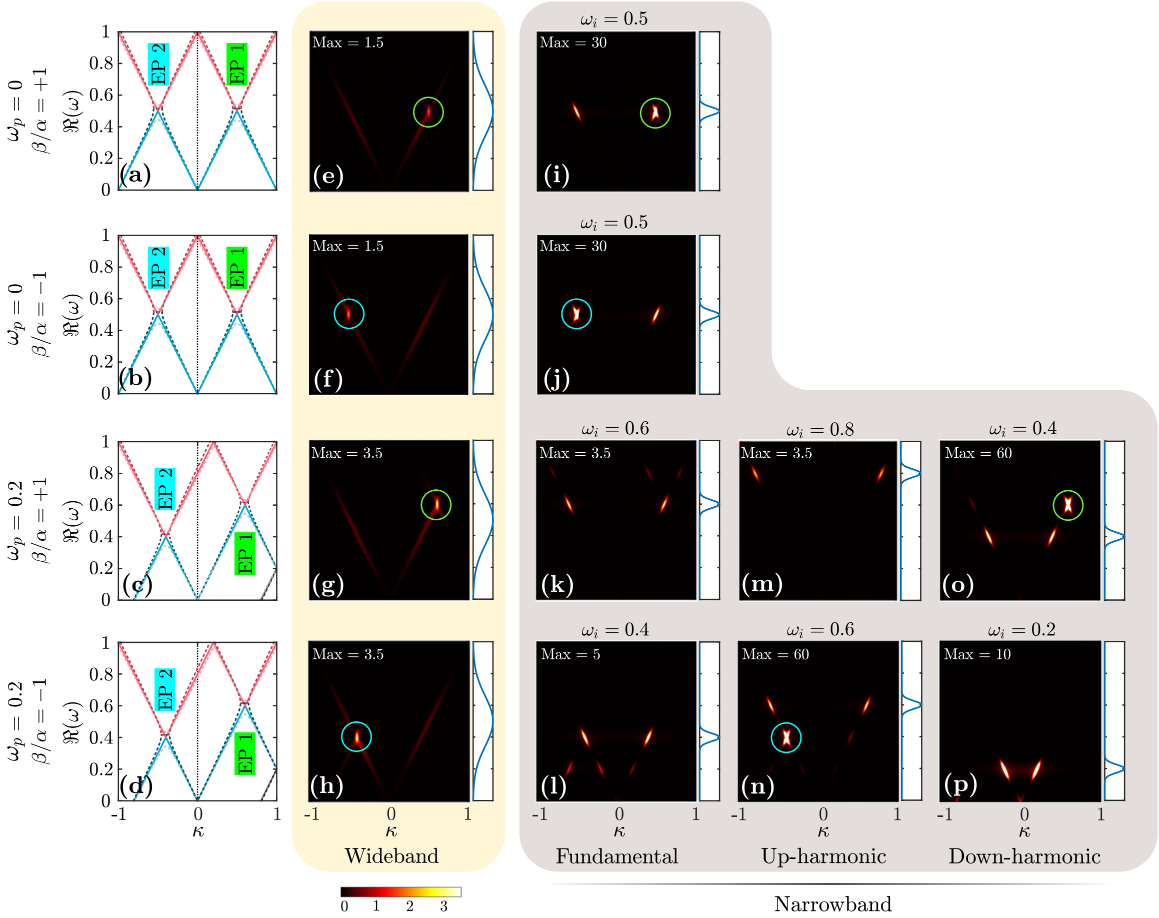

FIG. 9. Directional amplification at EPs. (a-d) $\Re(\omega)$-κ dispersion diagrams highlighting the location of EP 1 and EP 2 for (a) $\omega_p = 0$ and $\beta/\alpha = +1$, (b) $\omega_p = 0$ and $\beta/\alpha = -1$, (c) $\omega_p = 0.2$ and $\beta/\alpha = +1$, and (d) $\omega_p = 0.2$ and $\beta/\alpha = -1$. Solid lines in each figure show the dispersion bands at $|\beta/\alpha| = 1$ while dashed lines show the transition from $|\beta/\alpha| < 1$ to $|\beta/\alpha| > 1$. (e-h) Numerically constructed dispersion contours from the system's response to a wideband excitation. Excitation waveform is provided alongside the figure for visualization. Amplification at the location of EP 1 or EP 2 is marked using green or blue circles, respectively. (i-l) Numerically constructed dispersion contours from the system's response to a narrowband excitation targeting the frequency of the amplified EP shown in (e-h), i.e., $\omega_i = \omega_{\mathrm{EP/amp}}$. (m-n) Numerically constructed dispersion contours from the system's response to a narrowband excitation targeting the first up-harmonic of the amplified EP frequency shown in (g-h), i.e., $\omega_i = \omega_{\mathrm{EP/amp}} + \omega_p$. (o-p) Numerically constructed dispersion contours from the system's response to a narrowband excitation targeting the first down-harmonic of the amplified EP frequency shown in (g-h), i.e., $\omega_i = \omega_{\mathrm{EP/amp}} - \omega_p$. For comparison purposes, the color bar is kept unchanged throughout the figure while the maximum amplitude is listed on the top left corner of each case. System parameters used are: $\alpha = 0.2$, $\kappa_p = 1$, and $E_o = \rho_o = 1$.

which is consistent with the results obtained from Fig. 9. Furthermore, since $\tilde{u}_{-1}$ represents the down-harmonic component of the eigenvector as implied by the PWE solution in Eq. (7), this also explains why the EP amplification via a narrowband excitation was only attainable by targeting the down-harmonic of $\omega_{\mathrm{EP/amp}}$ in Fig. 9o. Similarly, in Fig. 10b, where $\beta/\alpha = -1$, a noticeable drop in the amplitude of $\tilde{u}_0$ is observed at $\kappa = -0.4$. Leading up to the same value of κ, a rise in the amplitude of $\tilde{u}_{+1}$ can also be observed. This is indicative of an amplification taking place at EP 2 (here at $\kappa = -0.4$) corresponding to $\beta/\alpha = -1$, which is consistent with the results obtained from Fig. 9. Furthermore, since $\tilde{u}_{+1}$ represents the up-harmonic component of the eigenvector, this explains why the EP amplification via a narrowband excitation was only attainable by targeting the up-harmonic of $\omega_{\mathrm{EP/amp}}$ in Fig. 9n. Finally, it is worth noting that the location of the EP remains unaltered regardless of the equal magnitudes of α and β, as can be inferred from the non-changing locations of the amplitude changes in $\tilde{u}_0$, $\tilde{u}_{-1}$, and $\tilde{u}_1$ in Fig. 10. However, the distribution of energy between different harmonics changes depending on the magnitude of α or β. Needless to mention, the observations made in this section can be generalized for all higher order harmonics (i.e., $\omega_{\mathrm{EP/amp}} \pm n\omega_p$ for $n \in \mathbb{Z}$ and $n \neq 0$).

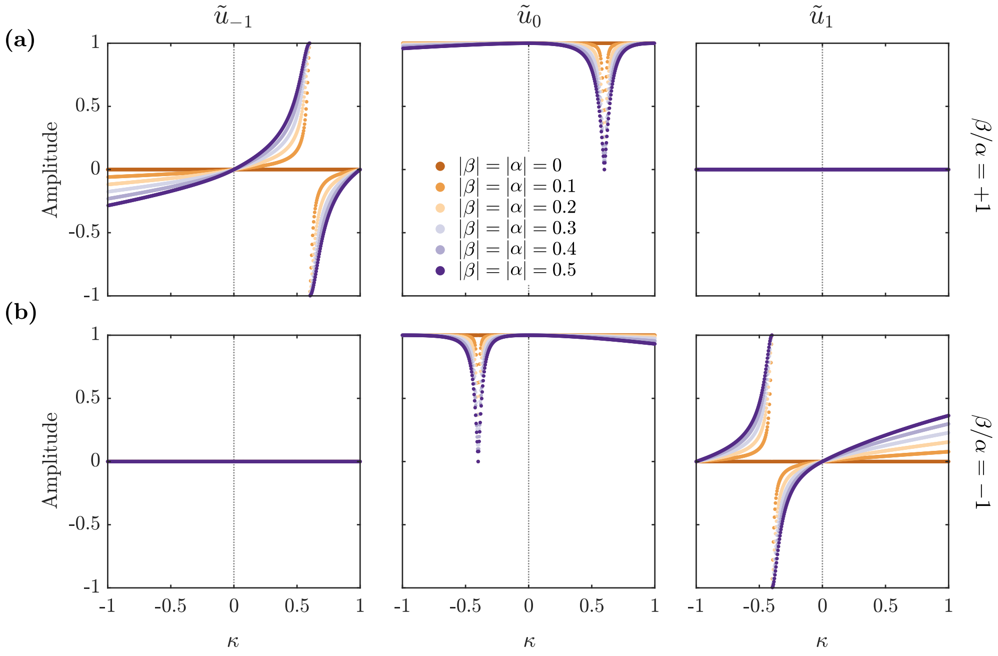

FIG. 10. Variation of the different components of the first eigenvector as a function of κ for different magnitudes of $|\beta| = |\alpha|$ with (a) $\beta/\alpha = +1$ and (b) $\beta/\alpha = -1$. $\tilde{u}_{-1}$ and $\tilde{u}_1$ denote the down- and up-harmonic components of the eigenvector, respectively, while $\tilde{u}_0$ represents fundamental component. System parameters used are: $\alpha = 0.2$, $\kappa_p = 1$, $\omega_p = 0.2$, and $E_o = \rho_o = 1$.

V. CONCLUSIONS

This work has investigated the wave dispersion mechanics of a one-dimensional elastic medium with a stiffness profile that is modulated using real (even) or imaginary (odd) space-time waveforms corresponding to different modulation speeds, each revealing intriguing features across the frequency and wavenumber axes, which can be summarized as follows: For even, real spatiotemporal modulations, either nonreciprocal PBGs or asymmetric κ-gaps form depending on whether the modulation speed ratio, ν, is smaller or greater than one. At the limit states of $\omega_p = 0$ or $\kappa_p = 0$, reciprocal PBGs or symmetric κ-gaps will be observed, respectively. For odd, imaginary spatiotemporal modulations, asymmetric odd-ordered κ-gaps form when $\nu < 1$, while a combination of nonreciprocal PBGs and asymmetric even-ordered κ-gaps form when $\nu > 1$. At the limit states of $\omega_p = 0$ or $\kappa_p = 0$, symmetric odd-ordered κ-gaps or a combination of reciprocal PBGs and symmetric even-ordered κ-gaps will be observed, respectively. The above takeaways were qualitatively captured by eight distinct examples, labeled Cases 1 through 8, which covered all the possible spatial, temporal, and spatiotemporal modulation profiles in both real and imaginary forms. The resultant behaviors of the systems undergoing these modulations are summarized in Table I.

Beyond the eight individually examined cases, the analysis of complex modulations with simultaneous real and imaginary components showed a large dependence on the absolute amplitude ratio $|\beta/\alpha|$, which revealed the following:

1. For a generalized complex stiffness modulation of the form $E(x,t) = E_o[1+\alpha\cos(\omega_p t - \kappa_p x) + \mathrm{i}\beta\sin(\omega_p t - \kappa_p x)]$, the dispersion behavior approaches that of a system with purely real modulations when $|\beta/\alpha| < 1$, and that of a system with purely imaginary modulations when $|\beta/\alpha| > 1$.

2. The $|\beta/\alpha| = 1$ system gives rise to a series of exceptional points (EPs) for both right- and left-going waves. Directional amplification will take place at the former EPs for positive values of β/α, and for the latter EPs for negative values of β/α. The frequency of the amplifiable EP is denoted $\omega_{\mathrm{EP/amp}}$.

Finally, unlike time-invariant non-Hermitian systems where EP amplification can be simply triggered with a narrow excitation of $\omega_{\mathrm{EP/amp}}$, the amplifiable EP in a non-Hermitian system with a temporal modulation $\omega_p \neq 0$ can be realized by exciting several harmonics of the amplifiable EP frequency, specifically $\omega_{\mathrm{EP/amp}} \mp n\omega_p$ for $\beta/\alpha = \pm 1$ (with $n \in \mathbb{Z}$ and $n \neq 0$); a feature which stems directly from the properties of the different components of the system eigenvectors. From a practical standpoint, the ability to trigger amplification at distinct frequencies, coupled with the significantly enhanced sensitivity to perturbations in the vicinity of EPs, can be extremely valuable given the rapidly increasing use of EPs in optical and acoustic sensing devices [55, 56]. In the presence of temporal modulations, EP-based sensors can therefore operate within a wider bandwidth since the amplification can be tuned to target multiple frequencies of interest spanning a broader range.

TABLE I. Summary of key features accompanying different stiffness modulation forms of a one-dimensional elastic medium. R, NR, S, and AS are abbreviations for reciprocal, nonreciprocal, symmetric, and asymmetric, respectively. /s denotes a shifting PBG at higher values of κ as demonstrated in Fig. 4.

Case	**Modulation**	**PBGs**	**κ-gaps**		
			Symmetry	Order	Level with increasing gap order
1	$\cos(-\kappa_p x)$	R	-	-	-
2	$\cos(\omega_p t)$	-	S	All	Decreasing
3	$\cos(\omega_p t - \kappa_p x)$; $\nu < 1$	NR	-	-	-
4	$\cos(\omega_p t - \kappa_p x)$; $\nu > 1$	-	AS	All	Decreasing
5	$\mathrm{i}\sin(-\kappa_p x)$	-	S	Odd	Constant
6	$\mathrm{i}\sin(\omega_p t)$	R/s	S	Even	Decreasing
7	$\mathrm{i}\sin(\omega_p t - \kappa_p x)$; $\nu < 1$	-	AS	Odd	Constant
8	$\mathrm{i}\sin(\omega_p t - \kappa_p x)$; $\nu > 1$	NR/s	AS	Even	Decreasing

ACKNOWLEDGMENTS

The authors acknowledges support of this work from the US National Science Foundation through award no. 1847254 (CAREER), as well as support from the University at Buffalo (SUNY) through the Buffalo Blue Sky Program.

[1] H. Nassar, B. Yousefzadeh, R. Fleury, M. Ruzzene, A. Alù, C. Daraio, A. N. Norris, G. Huang, and M. R. Haberman, Nonreciprocity in acoustic and elastic materials, Nat. Rev. Mater. **5**, 667 (2020).

[2] H. Al Ba'ba'a, M. Nouh, and T. Singh, Dispersion and topological characteristics of permutative polyatomic phononic crystals, Proc. Royal Soc. A **475**, 20190022 (2019).

[3] X. Su, Y. Gao, and Y. Zhou, The influence of material properties on the elastic band structures of one-dimensional functionally graded phononic crystals, J. Appl. Phys. **112**, 123503 (2012).

[4] M. Ansariand M. A. Karami, Analyzing the frequency band gap in functionally graded materials with harmonically varying material properties, in *Proc. SPIE* (International Society for Optics and Photonics, 2017) pp. 101701J–101701J.

[5] G. Trainiti, Y. Xia, J. Marconi, G. Cazzulani, A. Erturk, and M. Ruzzene, Time-periodic stiffness modulation in elastic metamaterials for selective wave filtering: Theory and experiment, Phys. Rev. Lett. **122**, 124301 (2019).

[6] J. Vila, R. K. Pal, M. Ruzzene, and G. Trainiti, A bloch-based procedure for dispersion analysis of lattices with periodic time-varying properties, J. Sound Vib. **406**, 363 (2017).

[7] H. Nassar, X. Xu, A. Norris, and G. Huang, Modulated phononic crystals: Non-reciprocal wave propagation and willis materials, J. Mech. Phys. Solids **101**, 10 (2017).

[8] M. A. Attarzadehand M. Nouh, Non-reciprocal elastic wave propagation in 2d phononic membranes with spatiotemporally varying material properties, J. Sound Vib. **422**, 264 (2018).

[9] G. Trainitiand M. Ruzzene, Non-reciprocal elastic wave propagation in spatiotemporal periodic structures, New J. Phys. **18**, 083047 (2016).

[10] M. A. Attarzadeh, H. Al Babaa, and M. Nouh, On the wave dispersion and non-reciprocal power flow in space-time traveling acoustic metamaterials, Appl. Acoust. **133**, 210 (2018).

[11] M. A. Attarzadeh, J. Callanan, and M. Nouh, Experimental observation of nonreciprocal waves in a resonant metamaterial beam, Phys. Rev. Appl. **13**, 021001 (2020).

[12] H. Nassar, H. Chen, A. Norris, M. Haberman, and G. Huang, Non-reciprocal wave propagation in modulated elastic metamaterials, Proc. Royal Soc. A **473**, 20170188 (2017).

[13] M. Ansari, M. Attarzadeh, M. Nouh, and M. A. Karami, Application of magnetoelastic materials in spatiotemporally modulated phononic crystals for nonreciprocal wave propagation, Smart Mater. Struct. **27**, 015030 (2017).

[14] J. Huangand X. Zhou, A time-varying mass metamaterial for non-reciprocal wave propagation, Int. J. Solids Struct. **164**, 25 (2019).

[15] J. Huangand X. Zhou, Non-reciprocal metamaterials with simultaneously time-varying stiffness and mass, J. Appl. Mech. **87**, 071003 (2020).

[16] M. A. Attarzadeh, S. Maleki, J. Crassidis, and M. Nouh, Non-reciprocal wave phenomena in energy self-reliant gyric metamaterials, J. Acoust. Soc. Am. **146**, 789 (2019).

[17] E. Riva, Harnessing $\mathcal{PT}$-symmetry in non-hermitian stiffness-modulated waveguides, Phys. Rev. B **105**, 224314 (2022).

[18] C. M. Benderand S. Boettcher, Real spectra in non-hermitian hamiltonians having pt symmetry, Phys. Rev. Lett. **80**, 5243 (1998).

[19] W. Wangand A. V. Amirkhizi, Exceptional points and scattering of discrete mechanical metamaterials, Eur. Phys. J. Plus **137**, 1 (2022).

[20] Ş. K. Özdemir, S. Rotter, F. Nori, and L. Yang, Parity–time symmetry and exceptional points in photonics, Nat. Mater. **18**, 783 (2019).

[21] K. G. Makris, R. El-Ganainy, D. N. Christodoulides, and Z. H. Musslimani, Pt-symmetric optical lattices, Phys. Rev. A **81**, 063807 (2010).

[22] M. Miri, A. B. Aceves, T. Kottos, V. Kovanis, and D. N. Christodoulides, Bragg solitons in nonlinear pt-symmetric periodic potentials, Phys. Rev. A **86**, 033801 (2012).

[23] M. C. Zheng, *Non-Hermitian Dynamics: Example from Disordered Microwave Cavities and Classical Optics*, Master's thesis, Wesleyan University (2009).

[24] W. Yang, Z. Yang, A. Guan, X. Zou, and J. Cheng, Design and experimental demonstration of effective acoustic gain medium for pt-symmetric refractive index, Appl. Phys. Lett. **120**, 063503 (2022).

[25] Z. Gu, H. Gao, P. Cao, T. Liu, X. Zhu, and J. Zhu, Controlling sound in non-hermitian acoustic systems, Phys. Rev. Appl. **16**, 057001 (2021).

[26] X. Zhu, H. Ramezani, C. Shi, J. Zhu, and X. Zhang, P t-symmetric acoustics, Phys. Rev. X **4**, 031042 (2014).

[27] L. Geng, W. Zhang, X. Zhang, and X. Zhou, Chiral mode transfer of symmetry-broken states in anti-parity-time-symmetric mechanical system, Proc. Royal Soc. A **477**, 20210641 (2021).

[28] J. Christensen, M. Willatzen, V. Velasco, and M.-H. Lu, Parity-time synthetic phononic media, Phys. Rev. Lett. **116**, 207601 (2016).

[29] D. Braghini, L. G. Villani, M. I. Rosa, and J. R. de F Arruda, Non-hermitian elastic waveguides with piezoelectric feedback actuation: non-reciprocal bands and skin modes, J. Phys. D: Appl. Phys. **54**, 285302 (2021).

[30] L. Feng, Y. Xu, W. S. Fegadolli, M. Lu, J. E. Oliveira, V. R. Almeida, Y. Chen, and A. Scherer, Experimental demonstration of a unidirectional reflectionless parity-time metamaterial at optical frequencies, Nat. Mater. **12**, 108 (2013).

[31] L. Ge, Y. Chong, S. Rotter, H. E. Türeci, and A. D. Stone, Unconventional modes in lasers with spatially varying gain and loss, Phys. Rev. A **84**, 023820 (2011).

[32] H. Hodaei, M. Miri, M. Heinrich, D. N. Christodoulides, and M. Khajavikhan, Parity-time–symmetric microring lasers, Science **346**, 975 (2014).

[33] A. E. Miroshnichenko, B. A. Malomed, and Y. S. Kivshar, Nonlinearly pt-symmetric systems: Spontaneous symmetry breaking and transmission resonances, Phys. Rev. A **84**, 012123 (2011).

[34] C. E. Rüter, K. G. Makris, R. El-Ganainy, D. N. Christodoulides, M. Segev, and D. Kip, Observation of parity–time symmetry in optics, Nat. Phys. **6**, 192 (2010).

[35] L. Chang, X. Jiang, S. Hua, C. Yang, J. Wen, L. Jiang, G. Li, G. Wang, and M. Xiao, Parity–time symmetry and variable optical isolation in active–passive-coupled microresonators, Nat. Photon. **8**, 524 (2014).

[36] R. Fleury, D. Sounas, and A. Alu, An invisible acoustic sensor based on parity-time symmetry, Nat. Commun. **6**, 1 (2015).

[37] H. Li, H. Moussa, D. Sounas, and A. Alù, Parity-time symmetry based on time modulation, Phys. Rev. Appl. **14**, 031002 (2020).

[38] A. Y. Song, Y. Shi, Q. Lin, and S. Fan, Direction-dependent parity-time phase transition and nonreciprocal amplification with dynamic gain-loss modulation, Phys. Rev. A **99**, 013824 (2019).

[39] Q. Liu, C. Qin, B. Wang, and P. Lu, Scattering singularities of optical waveguides under complex modulation, Phys. Rev. A **101**, 033818 (2020).

[40] N. Wang, Z. Zhang, and C. T. Chan, Photonic floquet media with a complex time-periodic permittivity, Phys. Rev. B **98**, 085142 (2018).

[41] T. T. Koutserimpas, A. Alù, and R. Fleury, Parametric amplification and bidirectional invisibility in pt-symmetric time-floquet systems, Phys. Rev. A **97**, 013839 (2018).

[42] Q. Wu, Y. Chen, and G. Huang, Asymmetric scattering of flexural waves in a parity-time symmetric metamaterial beam, J. Acoust. Soc. Am. **146**, 850 (2019).

[43] J. Parkand B. Min, Spatiotemporal plane wave expansion method for arbitrary space–time periodic photonic media, Opt. Lett. **46**, 484 (2021).

[44] A. Khelif, B. Aoubiza, S. Mohammadi, A. Adibi, and V. Laude, Complete band gaps in two-dimensional phononic crystal slabs, Phys. Rev. E **74**, 046610 (2006).

[45] J. Hsuand T. Wu, Efficient formulation for band-structure calculations of two-dimensional phononic-crystal plates, Phys. Rev. B **74**, 144303 (2006).

[46] V. Laude, B. Aoubiza, Y. Achaoui, S. Benchabane, and A. Khelif, Evanescent bloch waves in phononic crystals, in *Proc. SPIE*, Vol. 7223 (International Society for Optics and Photonics, 2009) p. 72230E.

[47] H. Al Ba'ba'a, M. Nouh, and T. Singh, Pole distribution in finite phononic crystals: Understanding bragg-effects through closed-form system dynamics, J. Acoust. Soc. Am. **142**, 1399 (2017).

[48] H. Al Ba'ba'aand M. Nouh, An investigation of vibrational power flow in one-dimensional dissipative phononic structures, J. Vib. Acoust. **139**, 021003 (2017).

[49] M. V. Bastawrousand M. I. Hussein, Closed-form existence conditions for bandgap resonances in a finite periodic chain under general boundary conditions, J. Acoust. Soc. Am. **151**, 286 (2022).

[50] F. Tisseurand K. Meerbergen, The quadratic eigenvalue problem, SIAM review **43**, 235 (2001).

[51] E. Galiffi, P. Huidobro, and J. B. Pendry, Broadband nonreciprocal amplification in luminal metamaterials, Phys. Rev. Lett. **123**, 206101 (2019).

[52] E. Cassedy, Temporal instabilities in traveling-wave parametric amplifiers (correspondence), IEEE Trans. Microw. Theory Tech. **10**, 86 (1962).

[53] E. Cassedy, Dispersion relations in time-space periodic media: Part ii, unstable interactions, Proc. IEEE **55**, 1154 (1967).

[54] M. Moghaddaszadeh, R. Adlakha, M. A. Attarzadeh, A. Aref, and M. Nouh, Nonreciprocal elastic wave beaming in dynamic phased arrays, Phys. Rev. Appl. **16**, 034033 (2021).

[55] J. Wiersig, Review of exceptional point-based sensors, Photonics Res. **8**, 1457 (2020).

[56] M. I. Rosa, M. Mazzotti, and M. Ruzzene, Exceptional points and enhanced sensitivity in pt-symmetric continuous elastic media, J. Mech. Phys. Solids **149**, 104325 (2021).